Effective magnetic correlations in hole-doped graphene nanoflakes

A. Valli,[1,*] A. Amaricci,[1] A. Toschi,[2] T. Saha-Dasgupta,[3] K. Held,[2] and M. Capone[1]

[1]*Democritos National Simulation Center, Consiglio Nazionale delle Ricerche, Istituto Officina dei Materiali (CNR-IOM) and Scuola Internazionale Superiore di Studi Avanzati (SISSA), Via Bonomea 265, 34136 Trieste, Italy*

[2]*Institut für Festkörperphysik, Technische Universität Wien, 1040 Vienna, Austria*

[3]*S. N. Bose National Centre for Basic Sciences, 70098 Kolkata, India*

(Received 9 October 2016; revised manuscript received 7 December 2016; published 29 December 2016)

The magnetic properties of zigzag graphene nanoflakes (ZGNFs) are investigated within the framework of inhomogeneous dynamical mean-field theory. At half-filling and for realistic values of the local interaction, the ZGNF is in a fully compensated antiferromagnetic (AF) state, which is found to be robust against temperature fluctuations. Introducing charge carriers in the AF background drives the ZGNF metallic and stabilizes a magnetic state with a net uncompensated moment at low temperatures. The change in magnetism is ascribed to the delocalization of the doped holes in the proximity of the edges, which mediate ferromagnetic correlations between the localized magnetic moments. Depending on the hole concentration, the magnetic transition may display a pronounced hysteresis over a wide range of temperatures, indicating the coexistence of magnetic states with different symmetries. This suggests the possibility of achieving electrostatic control of the magnetic state of ZGNFs to realize a switchable spintronic device.

DOI: 10.1103/PhysRevB.94.245146

I. INTRODUCTION

Graphene is widely regarded as a promising material for nanoelectronics [1]. The high electron mobility of the delocalized π electrons in graphene results in excellent electric and thermal transport properties, leading to the belief that graphene holds the potential to outperform Si for realization of high-speed and high-frequency response transistors and large-scale integrated circuits with a low environmental impact. In this respect, the semimetallic nature of graphene is not ideal for electronic applications and represents the main limitation to the realization of a graphene transistor. This issue can be overcome when considering nanostructured subunits of graphene: zero-dimensional graphene nanoflake (GNFs) and their one-dimensional counterparts, graphene nanoribbons (GNRs), which display a semiconducting gap strongly dependent on the system's size [1,2]. Particularly interesting is the role of the topology of the edge termination of graphene nanostructures in the stabilization of a magnetic state. Graphene zigzag (ZZ) edges have a defined chirality and consist of atoms belonging to the same triangular sublattice of graphene, while in armchair (AC) edges atoms of both sublattices are always paired. The imbalance at the ZZ edges is believed to be the origin of magnetism. This feature raised the interest in graphene applications also in the field of spintronics.

Recent experimental evidence [3–6] supports the idea that magnetism can be intrinsic in graphene nanostructures, and exceptionally high Néel temperatures up to room temperature have been reported [6]. In general, the experimental observation of magnetic states in graphene nanostructures remains scarce and controversial, and one of the main difficulties in the realization of long-range magnetic structures resides in the growth and in the intrinsic irregularity of the sample edges [5]. However, in the last few years, we have witnessed important advances in the synthesis and in the characterization of graphene nanostructures, e.g., at the interface with boron nitride [7,8], and the fingerprints of atomically precise edges have been uniquely identified in the Raman spectra of GNRs [9], paving the path toward graphene nanoelectronics.

From the theoretical point of view there is a substantial agreement on the phenomenon of edge magnetism within the framework of density functional theory (DFT) [10–14] and the mean-field approximation of the Hubbard model [15–17]. In particular, it has been proposed that the magnetic states of graphene nanostructures can be exploited for the realization of spintronic devices, e.g., spin filters [12,13,18,19] and logic gates [16,20] with graphene functional blocks. Recent investigations [14,21] suggested that the magnetic ordering of the ZZ edges in GNFs can be tuned by carrier doping. The presence of delocalized charge carriers entails ferromagnetic (FM) correlations, giving rise to a complex magnetic phase diagram. Indeed, it has been shown that the correlations between spatially separated magnetic impurities adsorbed on graphene can be interpreted in terms of a Rudermann-Kasuya-Kittel-Yoshida (RKKY) exchange interaction mediated by the π electrons of the graphene substrate [22–26].

Besides a few relevant exceptions [21,22,27–30], the role of electronic correlations beyond mean-field theory (MFT) in graphene nanostructures remains widely unexplored. This calls for a better theoretical understanding of the effects of electronic correlations on the magnetic properties and the interplay between charge and spin degrees of freedom in the presence of ZZ edges. We address this question in the framework of inhomogeneous dynamical mean-field theory (DMFT) [31], which is able to describe the interplay between the low-energy coherent excitations, arising due to the delocalization of the charge carriers on the lattice, and the incoherent high-energy excitations, related to the formation of the fluctuating local moment due to the Coulomb interaction.

The paper is organized as follows. In Sec. II A we discuss a Hubbard-model description of GNFs, while in Secs. II B and II C we show how DMFT allows us to investigate the magnetic properties of GNFs in the presence of electronic correlations.

*Corresponding author: angelo.valli@gmail.com

In Sec. III we present our numerical results. We focus on the case of a hexagonal ZGNF and discuss the onset of magnetism at half-filling as well as the interplay between charge and spin degrees of freedom at finite doping. Finally, Sec. IV provides our conclusion and outlook.

II. MODEL AND METHODS

A. Low-energy π-electrons Hamiltonian for GNFs

In graphene, the in-plane C-C bonds are formed due to an sp^2 hybridization between carbon s, p_x, and p_y atomic orbitals, while the p_z orbitals are perpendicular to the sp^2 bonds and form π orbitals that extend over the plane. Hence, in order to describe a GNF we can consider the following Hubbard Hamiltonian as an effective low-energy model for the delocalized π electrons on a finite-size honeycomb lattice with N sites:

$$\mathcal{H} = -\sum_{ij\sigma} t_{ij} c^{\dagger}_{i\sigma} c_{j\sigma} - \mu \sum_{i\sigma} c^{\dagger}_{i\sigma} c_{i\sigma} + U \sum_{i} n_{i\uparrow} n_{i\downarrow}. \quad (1)$$

In this notation, the operator $c^{(\dagger)}_{i\sigma}$ annihilates (creates) a π electron at site i with spin σ and $n_{i\sigma} = c^{\dagger}_{i\sigma} c_{i\sigma}$ is the corresponding number operator; t_{ij} are the tight-binding hopping parameters, μ is the chemical potential, and U denotes the local Coulomb repulsion.

The information on the spatial arrangement of the C atoms in the nanostructure is contained in the real-space hopping matrix, including also the topology of the edges (either ZZ or AC). Here, we restrict ourselves to the case of the hexagonal ZGNF shown in Fig. 1, while spatial symmetries are discussed in detail in Sec. II C. We assume a homogeneous hopping $t_{ij} = t$, where the nearest-neighbor (NN) hopping amplitude

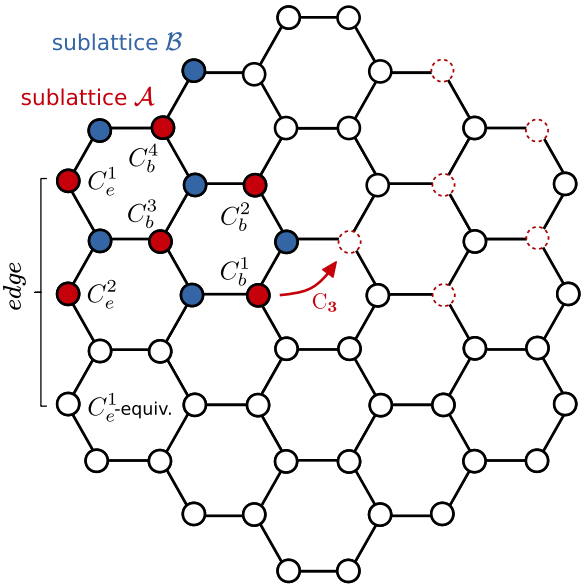

FIG. 1. Schematic of the hexagonal ZGNF considered. The $N_{\text{ineq}} = 6$ inequivalent C atoms are distinguished into bulk ($C_b^{1,\dots,4}$) and edge ($C_e^{1,2}$) atoms for each sublattice $\mathcal{A}$ (red circles) and sublattice $\mathcal{B}$ (cyan circles). The rotational symmetry C_3 sends all inequivalent atoms to their equivalent atoms on the same sublattice, indicated by dashed circles.

$t \equiv 1$ sets the energy scale of the system, and we neglect hopping processes beyond NN. Recently, Kretinin *et al.* [33] experimentally estimated the value of the next-NN hopping parameter in graphene to be $t'/t \approx 0.1$. While the presence of t' has important consequences such as breaking the particle-hole symmetry of the Hamiltonian, it was concluded that the asymmetry leads to relatively weak effects in the optical, as well as in the electronic, and presumably spin transport properties of monolayer graphene [33]. A configuration with spatially uniform hopping parameters is representative of the case where all the dangling C-C bonds at the ZZ edges are passivated, e.g., with hydrogen atoms. Within DFT it was shown that passivation quenches the edge magnetic moments significantly, while the lack of passivation changes the sp^2 hybridization between C atoms and induces sizable lattice distortions, mostly at the edges but also in the bulk [14]. A full structure relaxation allows one to derive the DFT tight-binding parameters, i.e., the hopping amplitudes and the local crystal fields of the distorted structure. However, according to the numerical results, in both the neutral and the hole-doped cases (and in contrast to the electron-doped one), the ZGNF does not display sizable lattice distortions, and the doped charges are distributed symmetrically over the edges [14]. In the following analysis we focus on hole-doped ZGNFs in order to study the interplay between charge and spin degrees of freedom in the stabilization of different magnetic phases. Hence, we disregard the effects of lattice distortions, as we do not expect any qualitative change in the results obtained. Finally, we consider a local Coulomb interaction U between the delocalized π electrons. Recently, both local and nonlocal Coulomb repulsion terms have been estimated to be sizable in graphene [34], justifying the necessity of treating graphene beyond the tight-binding or mean-field approximation. Indeed, electronic correlations, as well as the interplay between local and nonlocal repulsive interactions, are expected to play an important role in the stabilization of different magnetic orders in graphene nanostructures [21]. In the following we focus on the dynamical correlation effects driven by the local repulsion U within the framework of DMFT [31]. Unless specified otherwise, we choose a typical value of $U = 3.75t$, in line with recent estimates for graphene [34,35]. Nonlocal interaction could be taken into account within DMFT by including in Hamiltonian (1) a mean-field term, $V_{ij} \sum_{\sigma} n_{i\sigma} (\langle n_{j\uparrow} \rangle + \langle n_{j\downarrow} \rangle)$. However, the presence of nonlocal repulsion favors charge modulation on the lattice [21] and possibly leads to the proliferation of ordered states, which makes this extension beyond the scope of the present work.

B. Real-space dynamical mean-field theory with magnetic symmetry breaking

DMFT is a well-established theoretical tool to take into account local electronic correlations nonperturbatively. Numerous extensions of DMFT have also been proposed in which the self-energy is local albeit site dependent, allowing one to deal with inhomogeneous [36–39] and nanoscopic [40–45] systems, where in general the translational symmetry is broken along one or more directions in space. Nonlocal electronic correlations beyond mean field are in general expected to be important in low-dimensional

systems. However, by means of comparative studies [45] with diagrammatic [46] extensions of DMFT built on the local two-particle vertex function [47], it has been demonstrated that sometimes reasonable insights into the electronic and transport properties of correlated nanostructures [40,42,45] are already gained at the DMFT level. In the following we briefly recall how DMFT is implemented for an inhomogeneous finite system, and we discuss how to handle magnetic phases within this framework. In the case of a finite system, one can map each site $i = 1, \ldots, N$ of the original many-body problem onto an auxiliary Anderson impurity model (AIM) embedded in a self-consistent bath determined by the rest of the system. The auxiliary AIM for the ith site is defined by the spin-dependent local dynamical Weiss field $\mathcal{G}_{0i\sigma}(\omega)$ in terms of the local element of the real-space Green's function $G_{ij\sigma}(\omega)$ of the whole system and the local self-energy $\Sigma_{i\sigma}(\omega)$ as

$$\mathcal{G}^{-1}_{0i\sigma}(\omega) = G^{-1}_{ii\sigma}(\omega) + \Sigma_{i\sigma}(\omega). \tag{2}$$

In general, the local problems defined by $\mathcal{G}^{-1}_{0i\sigma}(\omega)$ are inequivalent, and each of them can be solved numerically, yielding a local dynamical self-energy $\Sigma_i(\omega)$ which carries a spatial dependence on the site index i. However, one can exploit any spatial symmetry of the original system and reduce the numerical effort by solving, eventually, only a subset of $N_{\text{ineq}} \leqslant N$ inequivalent local problems. This reduces the complexity of the problem from exponential in N to linear in N_{ineq}. The knowledge of all (inequivalent) $\Sigma_i(\omega)$ allows one to compute the Green's function of the whole system from the real-space Dyson equation

$$G^{-1}_{ij\sigma}(\omega) = (\omega + \mu)\delta_{ij} - t_{ij} - \Sigma_{i\sigma}(\omega)\delta_{ij}, \tag{3}$$

where the self-energy matrix contains only the local, site-dependent elements. Nonlocal correlations between different sites are neglected. From the Green's function one can define a new set of auxiliary AIMs and iterate the above process self-consistently until convergence.

In order to study the emergence of magnetism, we lift the local SU(2) spin rotational symmetry of the auxiliary AIM and allow the impurity solver to access solutions with a finite on-site magnetization $\langle S^z_i \rangle = \langle n_{i\uparrow} - n_{i\downarrow} \rangle$ (here we consider only solutions with magnetization in the z direction). This is done locally for each site i using a symmetry-broken Weiss field $\mathcal{G}_{0i\sigma}$ as initial input for the DMFT. In this respect, the separate treatment of the different spin directions is the only essential modification of the general self-consistent scheme of real-space DMFT, and in particular the self-consistent equations, whatever is the magnetic phase to be investigated, as opposed to the standard implementation of symmetry-broken solutions within DMFT [31]. The landscape of the possible magnetic phases that can be explored within this approach depends on the set of spatial symmetries enforced in the calculation and on the specific choice of the initial symmetry-breaking.

C. Spatial symmetries and magnetic phases of hexagonal ZGNFs

In the following we discuss in detail the spatial symmetries of hexagonal ZGNFs, which we enforce in order to investigate a landscape of possible magnetic configurations within the self-consistent DMFT calculations. We consider the hexagonal ZGNF shown in Fig. 1, which consists of a bipartite honeycomb lattice with $N = 54$ C atoms. Exploiting both the rotational symmetry of the C_{3v} point group and the sublattice symmetry, one can identify $N_{\text{ineq}} = 6$ inequivalent C atoms, all belonging to the same triangular sublattice (e.g., sublattice $\mathcal{A}$). The inequivalent C atoms can be further distinguished into bulk atoms (denoted C_b^{1-4}), which have three in-plane sp^2 C-C bonds, and edge atoms (denoted $C_e^{1,2}$), which have two C-C bonds and one dangling/passivated bond. A ZZ edge of the ZGNF consists of $N_{\text{edge}} = 3$ C atoms, i.e., two (equivalent) C_e^1 atoms and a C_e^2 atom, all belonging to the same sublattice. Neighboring edges consist of C atoms belonging to different sublattices, and are always connected by an AC bond between C_e^1 atoms. Lifting the local SU(2) spin rotational symmetry would be enough to study, e.g., (inhomogeneous) ferromagnetism. However, as the Hubbard model on a bipartite lattice has a natural tendency toward a Néel antiferromagnetic (AF) state (close to half-filling), a natural choice would be to enforce each kind of inequivalent atom to have opposite magnetization on different sublattices. However, this assumption would not allow other magnetic configurations, in particular, ferromagnetism. A more general description of the magnetic phases requires us instead to raise the number of inequivalent atoms in the system. Here we choose to lift the sublattice symmetry, i.e., treat each inequivalent atom and its counterpart in the other sublattice independently, thus raising N_{ineq}: $6 \rightarrow 12$. This choice allows us to stabilize either an AF or a FM state and describe the competition between the two short-range magnetic orders emerging from the interplay between charge and spin degrees of freedom at finite doping.

III. RESULTS AND DISCUSSION

In the following sections we discuss the onset of an AF insulating state of a ZGNF at half-filling. We also show that at finite doping there exists another magnetic state underneath the AF one, in which the magnetic moments at the ZZ edges are aligned FM. Such a state is unstable with respect to temperature fluctuations. We discuss the possible origin of the magnetic transition analyzing the effective magnetic exchange interaction mediated by the charge carriers.

A. ZGNF at half-filling

At half-filling, which corresponds to an average occupation of $\langle n \rangle = 1$ electron per site, and for passivated edges (i.e., in the case of homogeneous hopping parameters), Hamiltonian (1) is particle-hole symmetric and the density of states of the ZGNF is symmetric with respect to the chemical potential. Due to the discreteness of the spectrum, even in the absence of Coulomb interaction the system is semiconducting, with a charge gap $\Delta_0 \approx 0.7t$. The value of Δ_0 depends on the system's size and shape, and in particular, it has been shown both experimentally [48] and theoretically [14,49] that it decreases as $1/L$ with the linear size L of the GNF and vanish toward the semimetallic limit realized in bulk graphene.

We characterize the onset of the AF state at half-filling and at $T = 0$ by comparing the results obtained within static mean-field theory (MFT) and DMFT. In Fig. 2 we show the

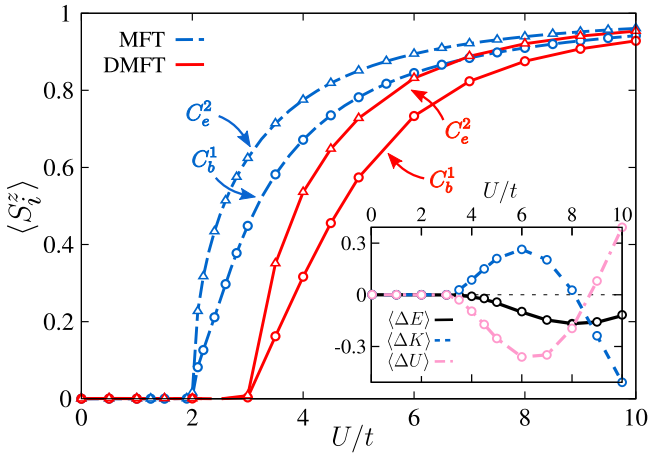

FIG. 2. Onset of AF order at $T = 0$ within static MFT (cyan symbols) and DMFT (red symbols). The local ordered magnetic moment $\langle S_i^z \rangle = \langle n_{i\uparrow} - n_{i\downarrow} \rangle$ for representative bulk C_b^1 and edge C_e^2 atoms displays a clear bulk-edge dichotomy. Inset: DMFT energy balance between the fully compensated AF and the PM phases. The total energy difference $\langle \Delta E \rangle = \langle H \rangle_{\rm AF} - \langle H \rangle_{\rm PM}$ is separated into kinetic $\langle \Delta K \rangle$ and potential energy $\langle \Delta U \rangle$ contributions.

local magnetic moment $\langle S_i^z \rangle = \langle n_{i\uparrow} - n_{i\downarrow} \rangle$ for representative atoms in the ZGNF, i.e., for bulk C_b^1 and edge C_e^2 atoms, as a function of the local interaction U/t. It is interesting to note that the onset of antiferromagnetism happens at a finite value of U/t and simultaneously for all inequivalent atoms, even though the size of the ordered moments of C_b^{1-4} (which are all similar yet not identical) is different from that of C_e^1 and C_e^2. Hence, we observe a clear *dichotomy* between bulk and edge atoms, even in the passivated case, which persists also when increasing the interaction. The resulting magnetic state is a fully compensated AF state but it is different from the conventional Néel state due to the inhomogeneous spatial distribution of the magnetic moments. Both static MFT and DMFT show the qualitative trend discussed above. Unsurprisingly, dynamical quantum effects suppress the AF phase, pushing the onset interaction toward the strong-coupling regime, i.e., from the value $U_{\rm AF} \approx 2t$ obtained within the static MFT to the value $U_{\rm AF} \approx 3t$ obtained within DMFT. Feldner *et al.* [27] have shown that the static MFT overestimates both the size of the local magnetic moment and the spectral gap of half-filled ZGNFs with respect to exact diagonalization and quantum Monte Carlo simulations. It is also interesting to note that the relative difference in size between the magnetic moment of bulk and that of edge atoms is enhanced within DMFT with respect to the static MFT. In fact, the spatial variation of the ordered local moment $\langle S_i^z \rangle$ can be traced back to a preformed (disordered) local moment in the paramagnetic (PM) state $\langle p_i \rangle = \langle (S_i^z)^2 \rangle = \langle n_{i\uparrow} + n_{i\downarrow} \rangle - 2\langle n_{i\uparrow} n_{i\downarrow} \rangle$, which already displays the bulk/edge dichotomy. In the magnetic state the value of $\langle p_i \rangle$ increases due to the decrease in double-occupation $\langle n_{i\uparrow} n_{i\downarrow} \rangle$, as each site stays locally half-filled, i.e., $\langle n_i \rangle = 1$. In the inset in Fig. 2 we show the DMFT energy balance as a function of U/t, where the internal energy difference between the fully compensated AF and the PM phases, i.e., $\langle \Delta E \rangle = \langle H \rangle_{\rm AF} - \langle H \rangle_{\rm PM}$ is separated into kinetic $\langle \Delta K \rangle$ and potential energy $\langle \Delta U \rangle$ contributions. For realistic values of the interaction parameter in graphene, the AF state is stabilized by a potential energy gain $\langle \Delta U \rangle < 0$ corresponding to the reduction in the double-occupation upon ordering. The above scenario mirrors the well-known DMFT picture [50–53] of the AF transition in the bulk Hubbard model, with its crossover from weak-to-strong coupling physics at values of U of the order of the bandwidth. This consideration would put any realistic value of the interaction in ZGNFs definitely on the weak-coupling (Slater) side. The main difference here is that the AF phase is not stabilized at arbitrary weak coupling, but it requires a finite onset interaction $U_{\rm AF}$ due to the semiconducting nature of the ZGNF at half-filling. Let us note that the value of the onset interaction depends on the size of the (correlated) spectral gap Δ in the PM phase, which shrinks with the linear size L of the ZGNF [48,49]. Thus ZGNFs of increasing size are expected to become magnetic at weaker interaction, while for small ZGNFs the onset interaction $U_{\rm AF}$ is dominated by finite-size effects. With a further increase in size, the semimetallic nature of graphene plays a role. In fact, even though $\Delta \to 0$, the lack of perfect nesting on the honeycomb lattice and the zero density of states at the Dirac point keep the onset interaction finite. Theoretical estimates of the onset interaction range from $U_{\rm AF} \approx 3.8t$ to $U_{\rm AF} \approx 4.5t$ with different numerical techniques [54–57], which seems to be in agreement with the experimental absence of antiferromagnetism in graphene monolayers.

It is interesting to discuss in detail the change in the low-energy spectral properties of the half-filled ZGNF across the magnetic transition. In Fig. 3 we show the occupied portion of the local spin-resolved spectral function $A(\omega < 0)$ for representative bulk C_b^1 and edge C_e^2 atoms. Due to the particle-hole symmetry, in the fully compensated AF state, the spectral function for spin σ fulfills the relation $A_\sigma(\omega > 0) = A_{\bar\sigma}(-\omega)$. We consider a local interaction $U = 3.75t$, which at $T = 0$ lies above but close to the DMFT onset value $U_{\rm AF}$ (see Fig. 2). In the absence of magnetism, the ZGNF in Fig. 3 is semiconducting, and the local spectral function (gray-shaded area) displays a spectral gap $\Delta \approx 0.5t$, where the gap is defined as the distance between the lowest energy peaks around the Fermi level. We note that the spectral gap Δ is substantially *reduced* by local electronic correlations with respect to the tight-binding value $\Delta_0 \approx 0.7t$, as expected in view of similar observations (within DMFT) in the insulating state of both bulk crystal [58] and molecules [45]. In the fully compensated AF phase we plot $A_\sigma(\omega)$ to show that the spin-$\uparrow$ and spin-$\downarrow$ spectral functions are inverted for the two sublattices. It is important to note that both the gap in the PM state Δ and the AF gap $\Delta^{\rm AF}$ do not display any spatial dependence on the ZGNF, despite the local magnetic moments of bulk and edge C atoms being different. This is shown in Fig. 4, where we plot the site-resolved spectral functions for all inequivalent atoms of sublattice $\mathcal{A}$ in the PM state (upper panel) and for both spin-$\uparrow$ and spin-$\downarrow$ polarizations in the fully compensated AF state (lower panel). The dashed vertical line indicates the position of the lowest energy peak for both spin polarizations. The right-hand panels also show the corresponding disordered local moment $\langle p_i \rangle$ and magnetic moment $\langle S_i^z \rangle$, respectively. The homogeneity of the spectral gap is the fingerprint of the separation between low-energy delocalized excitations and high-energy localized states in strongly correlated systems.

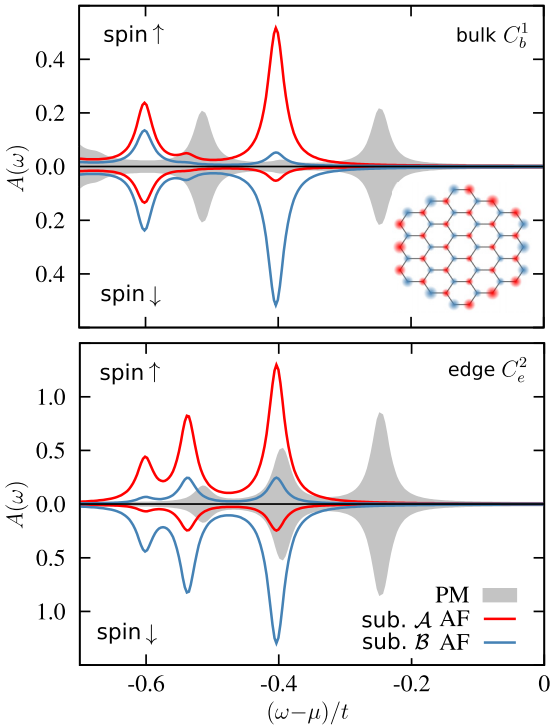

FIG. 3. Local spin-resolved DMFT spectral function $A(\omega)$ for bulk C_b^1 (upper panel) and edge C_e^2 (lower panel) atoms at $U/t = 3.75$, $\langle n\rangle = 1$, and $T = 0$. In the nonmagnetic calculation the ZGNF is a semiconductor (gray-shaded area), while the magnetic calculation yields a fully compensated AF insulating state, with opposite spin polarization in sublattices $\mathcal{A}$ (solid red line) and $\mathcal{B}$ (solid cyan line). Inset: Spatial distribution of the magnetic moments on the ZGNF; the color and the radius of the circles indicate the sign and the magnitude of $\langle S_i^z\rangle$.

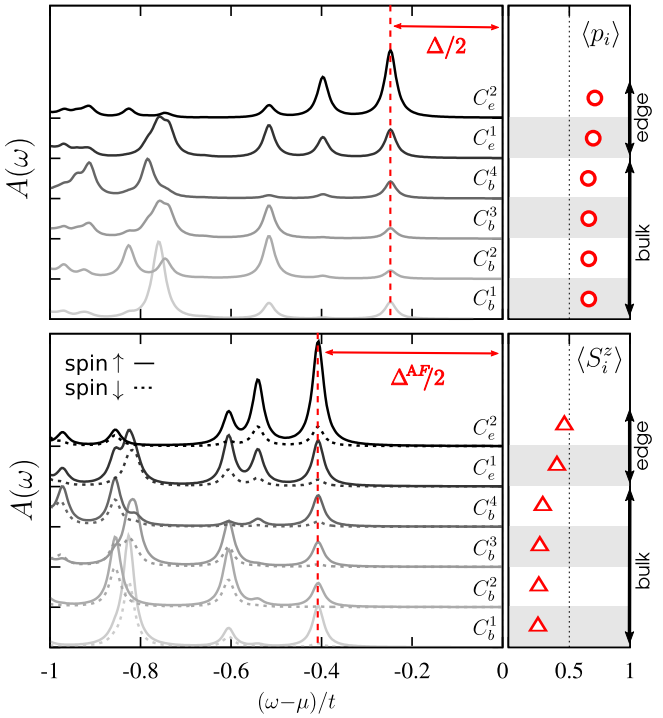

FIG. 4. Local spin-resolved DMFT spectral function $A(\omega)$ for all inequivalent C atoms in the PM (upper panel) and AF (lower panel) states at $U/t = 3.75$, $\langle n\rangle = 1$, and $T = 0$. The electronic coherence at low energy results in homogeneous spectral gaps Δ and Δ^{AF} (dashed vertical lines), despite the fact that the disordered $\langle p_i\rangle$ and ordered $\langle S_i^z\rangle$ local moments (open symbols in right-hand panels) display a clear bulk-edge dichotomy.

The high-energy properties follow the inhomogeneity dictated by the geometry or the single-particle potential to minimize the potential energy, while the low-energy properties, such as the spectral gap, are more homogeneous, as they are associated with a delocalized behavior which lowers the kinetic energy [59]. Concerning the spatial distribution of the magnetic moments, we can observe a modulation of the local magnetic moment also within each edge, as $\langle S_i^z\rangle$ is larger away from the corner, i.e., for C_e^2 atoms, as the C_e^1 atoms belonging to neighboring edges form an AC defect at each corner. While it has been shown [17,32] that magnetism at ZZ edges is robust against irregularities of the edge, such as AC defects, it is also true that the local magnetic moment is reduced, or even completely absent, at the armchair defects, as shown clearly, e.g., by Fernández-Rossier and Palacios [15]. Hence, the trend observed within DMFT for the $N_{\rm edge} = 3$ ZGNF (as well as for larger sizes, as in the case of $N_{\rm edge} = 4$ ZGNFs; not shown) is in agreement with other calculations in the literature. We can conclude that the linear size of the ZGNF that we have considered here is suitable to describe both the finite-size effects, which result in the physics being dominated by the ZZ edges, and the electronic features that would be expected in the bulk of an infinitely extended correlated system.

Extending the above analysis to finite temperatures, as also discussed in detail in the following section, we find the fully compensated AF state at half-filling to be stable up to room temperature $T_{\rm room}$ (see leftmost panel in Fig. 5). This observation is in agreement with recent experimental evidence in ZGNRs [6]. Moreover, the properties of the ordered state, in particular, the local magnetic moments $\langle S_i^z\rangle$, display a very weak dependence on T, sufficiently below the Neél temperature T_N.

B. Competing magnetic orders upon doping

In the following we explore the interplay between charge and spin degrees of freedom upon doping. As Hamiltonian (1) is particle-hole symmetric, hole and electron doping are equivalent in our model calculations. However, this is no longer the case if particle-hole symmetry is lifted. This is relevant, e.g., if one considers also a finite next-nearest-neighbor hopping, t', or takes into account inhomogeneous hopping parameters and on-site energies due to structural relaxations within DFT. Recent *ab initio* calculations showed that hole-doped ZGNFs display weak lattice distortions and that the doped charges are distributed symmetrically over the edges, in contrast with electron-doped ZGNF, which are instead heavily distorted, resulting also in a reduced symmetry with respect to the C_{3v} point group [14]. We do not expect a qualitative change in the general picture even without particle-hole symmetry. In particular, ferromagnetism may be induced by doped carriers

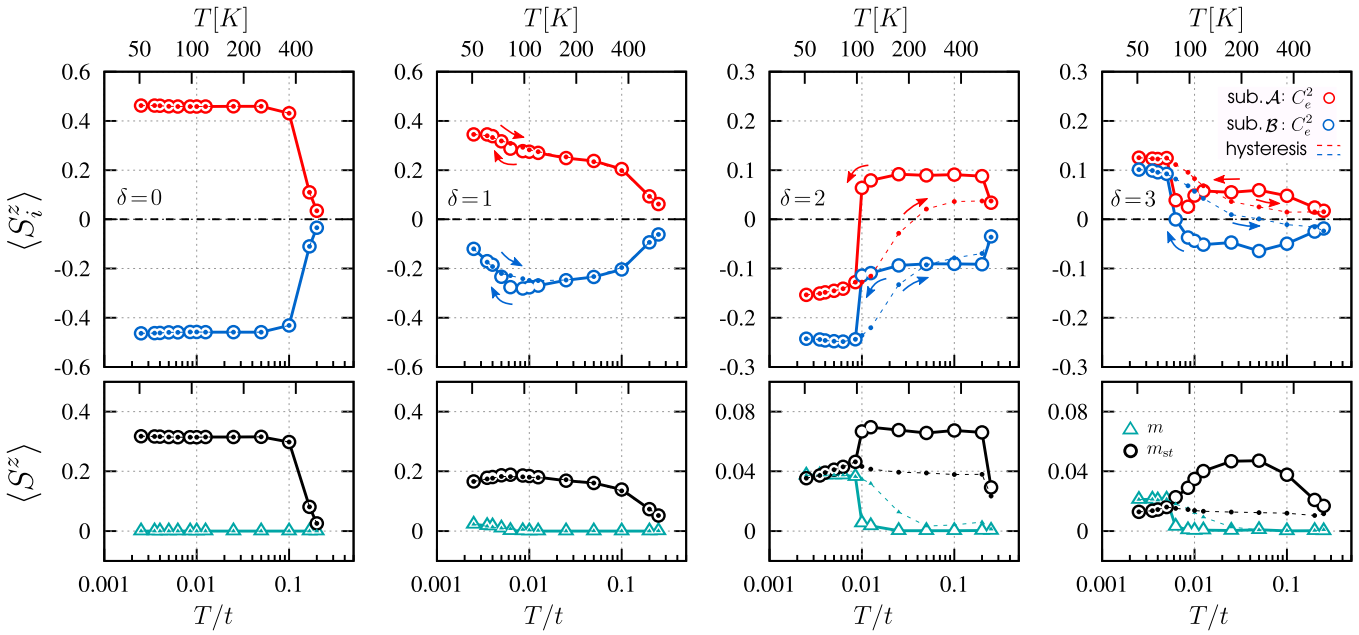

FIG. 5. Evolution of the magnetic moments in the ZGNF as a function of the temperature T/t at $U/t = 3.75$ and different values of doping δ. As a reference, the temperature scale (in K) is obtained by considering the realistic value $t = 2.7$ eV for the hopping parameter in graphene. Upper panels: Local magnetic moment $\langle S_i^z \rangle$ for the edge C_e^2 atoms in sublattice $\mathcal{A}$ (red symbols) and sublattice $\mathcal{B}$ (cyan symbols). Lower panels: Absolute value of the net magnetic moment m (jade triangles) and the staggered magnetization $m_{\rm st}$ (black circles) per atom in the ZGNF. The dashed line with filled symbols shows the hysteretic behavior of the magnetization.

with either charge. A quantitative difference to be expected is instead the doping concentration necessary to trigger the FM transition, which, in general, will be different for electrons and holes and will be strongly dependent on the details of the one-body Hamiltonian.

Charge carries can be introduced in the ZGNF, e.g., by using a gate electrode or by chemical substitution with carboxyl (COOH) or hydroxyl (OH) groups, which should not disrupt the sp^2 hybridization at the edges [60]. The most interesting result is that the fully compensated AF state is unstable upon doping, due to the emergence of ferromagnetic correlations between spins at the ZZ edges. We show that at finite doping and below a critical temperature T_c it is energetically favorable for the local magnetic moment $\langle S_i^z \rangle$ of the C_e^2 atoms to be aligned ferromagnetically both within the same edge and between neighboring edges, while bulk C atoms tend to maintain an AF pattern. The resulting magnetic state is characterized by an uncompensated net magnetic moment *and* a finite staggered magnetization. In the following we denote it the ferrimagnetic (FI) state, although we stress that the ZGNF does not display a proper FI order. A similar behavior upon doping was recently observed for the same ZGNF within DFT calculations at $T = 0$ [14].

The upper panels in Fig. 5 show the temperature evolution of the local magnetic moment $\langle S_i^z \rangle$ for the edge C_e^2 atoms of sublattices $\mathcal{A}$ and $\mathcal{B}$. We provide also reference values of T (in K) obtained with a typical value $t \approx 2.7$ eV for the hopping integral in bulk graphene. The doping is denoted δ, the integer number of holes in the ZGNF, so that nominal filling of the ZGNF is $n = (N - \delta)/N$. For all cases we considered, the magnetic state in the high-T regime is the fully compensated AF state. The orientation of the magnetic moment is opposite for atoms in different sublattices, giving rise, globally, to a staggered magnetization $m_{\rm st} = \frac{1}{N}\sum_{i=1}^{N} \langle S_i^z \rangle^i$. Away from half-filling and below a doping-dependent temperature $T_c(\delta)$ the system also develops a finite net magnetic moment $m = \frac{1}{N}\sum_{i=1}^{N} \langle S_i^z \rangle$ (uniform magnetization), which coexists with a finite $m_{\rm st}$, giving rise to an FI state. The results for the absolute value of the magnetic moments m and $m_{\rm st}$ are shown in the lower panels in Fig. 5 for each δ. At half-filling the fully compensated AF state is characterized by a Néel temperature $T_N \approx T_{\rm room}$ and does not display any tendency toward the FI state down to the lowest T explored. While the mean-field character of the spatial fluctuations within DMFT is known to overestimate the ordering temperature [61,62], the observation of a sizable T_N for edge magnetism is in agreement with recent experimental evidence in ZGNRs [6]. The annealing procedure at $\delta \neq 0$ shows that the ZGNF is driven away from a fully compensated AF state upon lowering T by breaking the spin inversion symmetry between the $\mathcal{A}$ and the $\mathcal{B}$ sublattices. In the case of one hole, i.e., $\delta = 1$ (second panel from left in Fig. 5), the local magnetic moment $\langle S_i^z \rangle$ for the C_e^2 atoms increases, as is to be expected, upon lowering T until the sublattice symmetry is broken at $T_c/t \approx 0.008$ ($T_c \approx 100$ K). Below T_c, the staggered magnetization $m_{\rm st}$ decreases and the ZGNF develops a net magnetic moment $m \neq 0$. The major contribution to m (and to the decrease in $m_{\rm st}$) is given by the asymmetry that develops between the magnetic moments of the C_e^2 atoms in the two sublattices. Let us stress once again that the magnetic transition happens *spontaneously* upon annealing, as the symmetries of the ZGNF enforced in the numerical calculation allow both the AF and the FM solutions, as well as the coexistence of the two orders. The situation is substantially different at higher hole concentrations. At

$\delta = 2$ (third panel from left in Fig. 5) the ZGNF displays a sudden change in the magnetic configuration at $T_c/t \approx 0.02$ ($T_c \approx 140$ K) from a high-T, fully compensated AF state to a low-T FI state. In the FI state all the inequivalent C_e^2 spins are aligned ferromagnetically, although they are not equal in size due to the breaking of the sublattice symmetry. The trend of the data at low T suggests that the sublattice asymmetry could possibly disappear in the limit $T \to 0$. Away from the transition, the properties of the ZGNF are nearly independent of T up to a sharp drop above T_{room}. A similar behavior is found at $\delta = 3$ (rightmost panel in Fig. 5). We can estimate the transition temperature to $T_c \approx 100$ K, which turns out to be lower than the one for $\delta = 2$. Interestingly, the effect in the bulk atoms in the ZGNF is weaker, although a clear discontinuity in the T dependence of the local magnetic moment can be observed for $\delta = 2$ and $\delta = 3$ (not shown).

At $\delta \neq 0$ the magnetization also displays a hysteretic behavior. The hysteresis is evident especially for $\delta = 2$ and $\delta = 3$, where it extends over a wide range of T and indicates the coexistence of short-range AF and FM orders. We note that both the local magnetic moments $\langle S_i^z \rangle$ decrease upon doping. While this is expected within DMFT, it is instead absent in reference $T = 0$ DFT calculations, where the spin density at the edges is the same in both the AF and the FI states [14].

It is interesting to relate the changes in the local magnetic moments at the ZZ edges across the AF-to-FI transition to the changes in the low-energy excitation in the spectral functions. To this end, we focus on the edge C_e^2 atoms of sublattices $\mathcal{A}$ and $\mathcal{B}$. The corresponding local spin-resolved spectral functions $A(\omega)$ in the PM and the magnetic (AF or FI) states are shown in Figs. 6 and 7 at $\delta = 2$ and $\delta = 3$, respectively. A common feature of doped ZGNFs is the metallic character of the spectrum due to the redistribution of spectral weight in the site-resolved $A(\omega)$ with respect to half-filling (compare with Fig. 3). We observe a resonance at the Fermi level, associated with the delocalization of the electrodoped charge carriers on the lattice. The low-energy coherent excitations at $\delta \neq 0$ coexist with the incoherent high-energy excitations (Hubbard bands) related to the formation of the fluctuating local moment due to the Coulomb interaction. In the magnetic state above $T_c(\delta)$ analysis of the spectral functions in (the upper panels in) Figs. 6 and 7 clearly indicates the AF alignment of the C_e^2 atoms in the different sublattices. Below T_c (lower panels) a redistribution of the low-energy spectral weight splits the spin-$\uparrow$ and spin-$\downarrow$ spectral functions with respect to the Fermi level, showing a tendency toward an insulating state. The splitting is the same for sublattices $\mathcal{A}$ and $\mathcal{B}$. As a consequence the local magnetic moments of the edge C_e^2 atoms in the two sublattices are aligned ferromagnetically. For $\delta = 2$ the sublattice asymmetry is evident, while for $\delta = 3$ it is minimal. The spatial distribution of the magnetic moments above and below T_c and the corresponding change in the magnetic pattern for both values of δ are shown in the respective insets.

In order to understand the nature of the magnetic correlations at the ZZ edges we analyze the spatial distributions of the holes upon doping. In the upper panel in Fig. 8 we show the local hole density for the bulk C_b^1 and edge C_e^2 atoms as a function of the average electron density $\langle n \rangle$ in

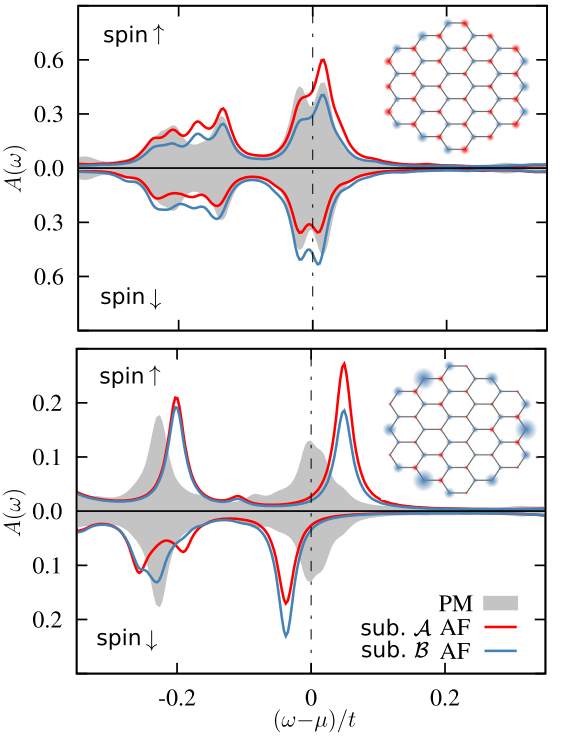

FIG. 6. Local spin-resolved DMFT spectral function $A(\omega)$ for the edge C_e^2 atoms at $U/t = 3.75$ and $\delta = 2$. Upper panel: fully compensated AF state at $T/t = 0.010$ ($T \approx 160$ K). Lower panel: FI state at $T/t = 0.005$ ($T \approx 80$ K). Color coding reads as in Fig. 3 for both panels and the inset.

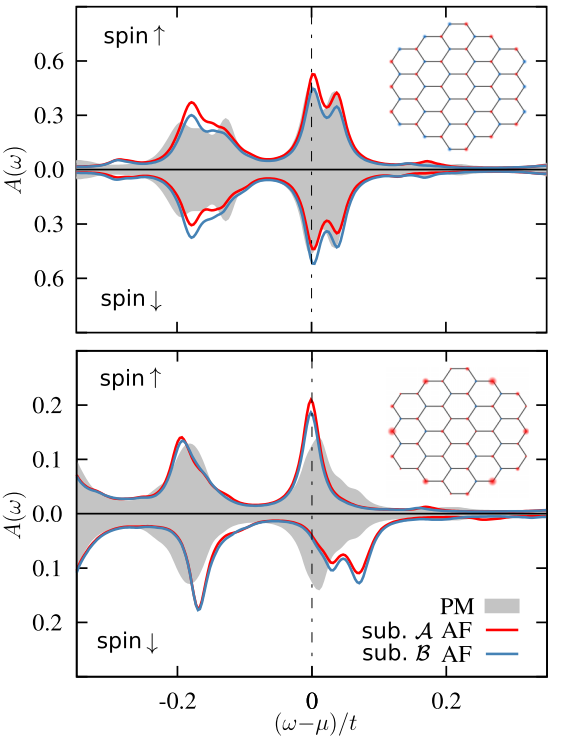

FIG. 7. As Fig. 6, but for $\delta = 3$, showing an FM alignment of the C_e^2 magnetic moments below T_c.

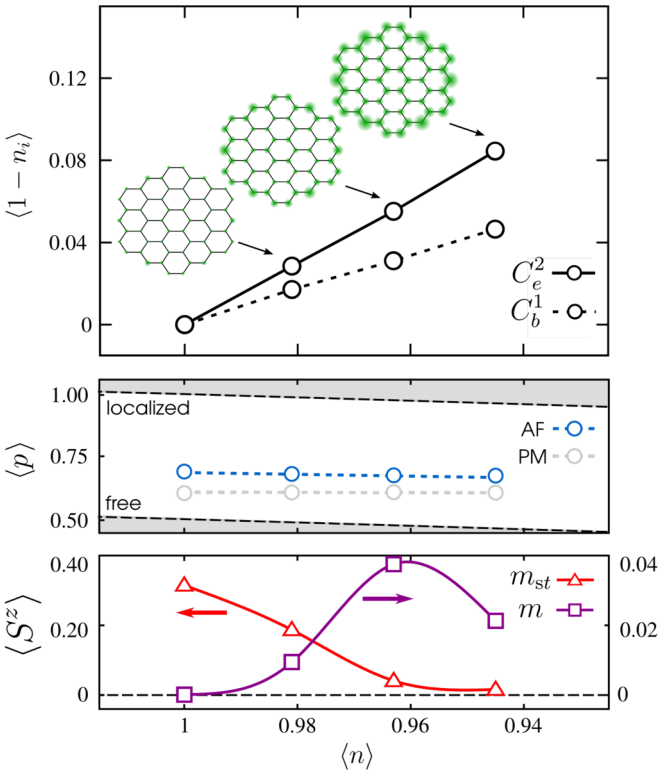

FIG. 8. Distribution and influence of doped holes as a function of the average electron density in the ZGNF $\langle n\rangle$ at $U/t = 3.75$ and $T/t = 0.005$ ($T \approx 80$ K). Upper panel: Local hole density $\langle 1 - n_i\rangle$ for the bulk C_b^1 and the edge C_e^2 atoms in the PM state. Insets: Spatial distribution of the holes in the ZGNF. Middle panel: Average fluctuating local moment $\langle p\rangle$. Dashed lines separating the shaded area correspond to the free and fully localized limits (see text for details). Lower panel: Absolute value of the net magnetic moment m and staggered magnetization $m_{\rm st}$.

the ZGNF. The holes are found to be localized mostly at the ZZ edges, and the ratio of the hole concentration at the edge to that in the bulk increases with doping. However, the average hole concentration on the lattice obtained within DMFT is less heterogeneous than in reference DFT calculations [14] due to the effects of the hole-hole repulsion at the edges. The hole concentration in Fig. 8 is shown for $T/t = 0.005$ ($T \approx 80$ K), which is below $T_c(\delta)$ for all $\delta \neq 0$, but the spatial distribution of the holes on the lattice is very weakly dependent on T (not shown). We also find that there is no sizable redistribution of the holes on the lattice between the PM and the magnetically ordered states, except for a slight asymmetry due to the sublattice symmetry breaking in the FI state. In the other two panels in Fig. 8, we show the evolution with doping of the average fluctuating local moment $\langle p\rangle = \frac{1}{N}\sum_i \langle p_i\rangle$ in relation to the magnetization m and $m_{\rm st}$ in the ordered state. Upon magnetic ordering, the value of $\langle p\rangle$ increases due to the reduction in double-occupations. At half-filling this corresponds to the gain in potential energy shown in the inset in Fig. 2. We note that $\langle p\rangle$ is weakly dependent on the doping. If we compare it with the value $\langle p\rangle$ in the uncorrelated (free) and the fully localized cases, where the local double-occupations are $\langle n_{i\uparrow}n_{i\downarrow}\rangle = 0.25$ and $\langle n_{i\uparrow}n_{i\downarrow}\rangle = 0$, respectively. We can conclude that $\langle p\rangle$ gets closer to the localized limit upon doping. At the same time the magnetization $m_{\rm st}$ is strongly suppressed in favor of an uncompensated magnetic moment m as FM correlations tend to align the magnetic moment at the ZZ edges. The net magnetic moment as a function of the doping $m(\delta)$ displays a dome shape, peaked at an optimal value of $\delta \approx 2$, which develops upon the lowering of T. Within the usual DMFT picture, the presence of a sizable *preformed* local moment, while the magnetic order is capped by a lower coherence energy scale, would indicate the realization of a strong-coupling scenario [50,51]. This suggests a crossover from weak- to strong-coupling magnetism in ZGNF upon doping away from half-filling. Based on these observations we can argue that the delocalized holes mediate an effective magnetic exchange interaction, which is dynamically generated between the magnetic moments localized at the edges. This mechanism ultimately leads to the change in the magnetic structure in the doped ZGNF. This highly nontrivial physics can indeed be captured by DMFT because it is able to describe both the coherent and the incoherent excitations as well as their interplay. Evidence in support of this claim is presented in Sec. III C, where we evaluate the effective magnetic exchange interaction.

C. Effective magnetic interactions

In the following we analyze the effective magnetic interactions generated by the interplay of the local repulsion U and the delocalization of electrons and holes in the ZGNF, which we argue to be the mechanism behind the stabilization of the FI state. Within the local self-energy approximation (as in DMFT), an estimate of the effective magnetic exchange interaction parameters J_{ij} can be obtained, following Katsnelson and Lichtenstein [63], as

$$J_{ij} = -\int_{\infty}^{\infty} d\omega \Sigma_i^s(\omega) G_{ij}^{\uparrow}(\omega) \Sigma_j^s(\omega) G_{ji}^{\downarrow}(\omega) f(\omega), \qquad (4)$$

where $f(\omega) = (e^{\beta(\omega-\mu)}+1)^{-1}$ is the Fermi distribution function at the inverse temperature $\beta = 1/T$, while $\Sigma_i^s = (\Sigma_i^{\uparrow} - \Sigma_i^{\downarrow})/2$ is the asymmetric spin combination of the local (dynamical) self-energy, and G_{ij}^{σ} is the real-space nonlocal Green's function connecting sites i and j, with spin σ. Diagrammatically, the effective exchange J_{ij} can be thought as the frequency convolution of the bubble term χ_{ij}^0 of the nonlocal susceptibility, with the nonlocal Green's function as the fermionic lines of the bubble and Σ_i^s playing the role of the local vertex. Let us stress that the coupling $J_{ij} = 0$ in the PM state (where $\Sigma_i^{\uparrow} = \Sigma_i^{\downarrow}$) and it should not be interpreted as the magnetic coupling of an effective spin lattice Hamiltonian (e.g., of the Heisenberg model), as it carries a temperature and doping dependence through both the Green's function and the self-energy. Rather, Eq. (4) resembles the typical expression [22,26] used to evaluate the RKKY exchange coupling between magnetic adatoms, $J_{\rm RKKY} \propto J^2\chi_{ij}^0$, where J couples the impurity spin with the spin density on the substrate, and χ_{ij}^0 is the static spin susceptibility of the conduction electrons, which mediate the effective magnetic interaction. In analogy, we have that Σ_i^s is associated with the presence of localized magnetic moments and the effective exchange

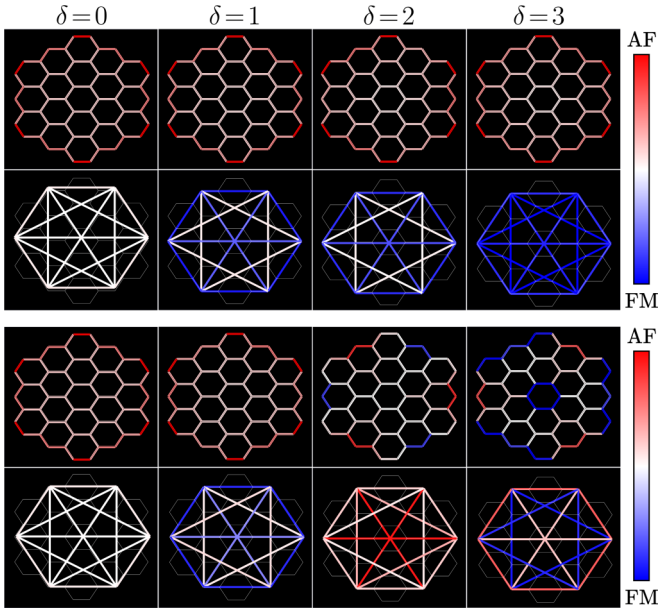

FIG. 9. Effective magnetic exchange J_{ij} between all NN pairs and edge C_e^2 atom pairs for different dopings. The color and the intensity of the links denote the nature and the strength of the magnetic interaction: from AF (red) to FM (blue). Data are normalized to the strongest J_{ij} for better visibility, while numerical values of the couplings are listed in Table I as a reference. Upper panels: AF state, at $T/t = 0.010$ ($T \approx 80$ K). Lower panels: FI state, at $T/t = 0.005$ ($T \approx 160$ K).

between them is mediated by the doped holes delocalized on the lattice.

The expression for J_{ij} in Eq. (4) yields the effective magnetic exchange for any pair (i, j) in the ZGNF. However, in order to highlight the microscopic mechanism behind the AF-to-FI magnetic transition, we focus on the magnetic exchange parameters between all NN atom pairs and all edge C_e^2 atom pairs. In Fig. 9 we show a graphical representation on the ZGNF of the values obtained for relevant magnetic exchange parameters J_{ij}. We show the data as a function of doping and for two values of temperature, $T/t = 0.010$ ($T \approx 160$ K) and $T/t = 0.005$ ($T \approx 80$ K), which are representative of the high-T (AF) and low-T (FI) magnetic states discussed above. At half-filling, we find all magnetic interactions $J_{ij} > 0$ (i.e., AF in nature). The short-range and, in particular, the NN interactions $J_{\rm NN}$ are stronger at the edges with respect to the bulk. The values of J_{ij} are rapidly suppressed with distance $|i - j|$, and in particular, long-range interactions between different edges are negligibly weak with respect to $J_{\rm NN}$ within a given edge. The magnetic properties at half-filling are weakly dependent on T (below T_N) and this is reflected also in the magnetic couplings. At finite doping and above T_c we find $J_{\rm NN} > 0$ and quantitatively similar to the values at $\delta = 0$ for all values of doping. However, the presence of delocalized charge carriers mediates sizable long-range magnetic interactions. Some of the long-range interactions connecting edge C_e^2 atoms, indicated as J_1, J_2, and J_3 in Table I, are found to be negative (i.e., FM in nature) at finite doping. Eventually, the presence of $J_{ij} < 0$ drives the onset of the FI state as $T \to T_c(\delta)$. Interestingly, below $T_c(\delta)$ the change in the magnetic structure at $\delta \neq 0$ is reflected also in a change in the effective exchange interactions. The results are clearer for $\delta = 2$ and $\delta = 3$, where an exact correspondence can be found between the $J_{\rm NN}$ shown in Fig. 9 and the relative orientation of the corresponding pair of magnetic moments shown, e.g., in the insets in Figs. 6 and 7, respectively. The behavior of long-range interactions is less obvious and better illustrated in Fig. 10, in which we compare the doping dependence of both representative $J_{\rm NN}$ and the J_{1-3} magnetic exchange interactions above and below T_c. In general, $J_{\rm NN}$ values become weaker upon doping, with some of them (in particular, at the ZZ edges) becoming FM at $\delta = 2$ and $\delta = 3$ below T_c. Instead, long-range interactions are enhanced at $\delta = 1$ with respect to the half-filling case but are suppressed upon further increase in the doping. The interactions J_1 and J_3, which connect edge C_e^2 atoms of different sublattices, are usually larger than J_2 and display an oscillatory behavior, changing sign as a function of the doping. In particular, the FM nature of $J_1 < 0$ and $J_3 < 0$ above T_c reveals the tendency of

TABLE I. Relevant effective magnetic interaction parameters J_{ij}/t [10^{-4}]. The long-range interactions J_1, J_2, and J_3 denote exchange between edge C_e^2 atoms belonging to neighboring, next-nearest neighboring, and opposite edges of the ZGNF, respectively. While J_1 and J_3 always connect C_e^2 atoms on different sublattices, J_2 connects C_e^2 atoms on the same sublattice and assumes different values if the sublattice symmetry is broken. Nearest-neighbor interactions J_{NN} denote exchange between C_b^1 pairs, C_e^1 pairs, or C_b^4-C_e^2 pairs. The latter assumes different values if the sublattice symmetry is broken. The above magnetic exchanges are also indicated graphically on the ZGNF in Fig. 9, for the sake of clarity.

	$T/t = 0.005$ ($T \approx 80$ K)				$T/t = 0.010$ ($T \approx 160$ K)			
	$J_1^{\mathcal{AB}}$	$J_2^{\mathcal{AA}}$	$J_2^{\mathcal{BB}}$	$J_3^{\mathcal{AB}}$	$J_1^{\mathcal{AB}}$	$J_2^{\mathcal{AA}}$	$J_2^{\mathcal{BB}}$	$J_3^{\mathcal{AB}}$
$\delta = 0$	0.38(5)	0.01(6)	0.01(6)	0.04(5)	0.38(4)	0.01(6)	0.01(6)	0.04(5)
$\delta = 1$	−0.34(9)	0.26(5)	0.17(1)	−1.08(5)	−0.21(9)	0.14(3)	0.14(5)	−0.75(7)
$\delta = 2$	0.05(9)	0.02(4)	0.02(5)	0.09(1)	−0.05(0)	0.00(6)	0.01(8)	−0.08(6)
$\delta = 3$	0.03(9)	−0.01(1)	0.01(5)	−0.00(6)	−0.01(4)	−0.00(1)	−0.00(1)	−0.00(1)
	$J_{\rm NN}^{\mathcal{AB}}$ C_b^1-C_b^1	$J_{\rm NN}^{\mathcal{AB}}$ C_e^1-C_e^1	$J_{\rm NN}^{\mathcal{AB}}$ C_b^4-C_e^2	$J_{\rm NN}^{\mathcal{BA}}$ C_b^4-C_e^2	$J_{\rm NN}^{\mathcal{AB}}$ C_b^1-C_b^1	$J_{\rm NN}^{\mathcal{AB}}$ C_e^1-C_e^1	$J_{\rm NN}^{\mathcal{AB}}$ C_b^4-C_e^2	$J_{\rm NN}^{\mathcal{BA}}$ C_b^4-C_e^2
$\delta = 0$	1.00(4)	5.52(4)	2.70(2)	2.70(9)	1.01(3)	5.47(1)	2.68(4)	2.69(3)
$\delta = 1$	0.26(2)	2.05(4)	0.77(0)	1.03(1)	0.27(0)	2.01(2)	0.91(6)	0.91(0)
$\delta = 2$	0.00(3)	0.02(5)	0.22(9)	−0.08(1)	0.02(6)	0.26(8)	0.13(7)	0.07(6)
$\delta = 3$	−0.00(1)	−0.00(6)	−0.02(0)	0.04(0)	0.00(7)	0.07(2)	0.02(7)	0.03(1)

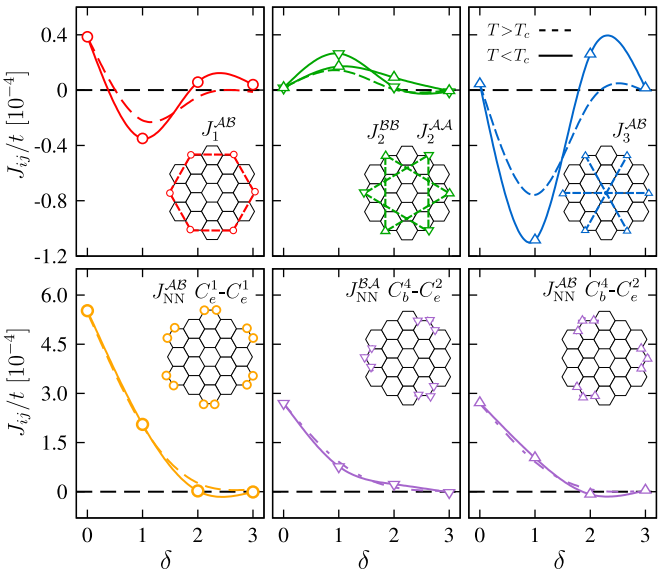

FIG. 10. Effective parameters for relevant magnetic interactions J_{ij} as a function of the doping δ. Dashed and solid lines (guides for the eye) with open symbols correspond to $T/t = 0.010$ ($T > T_c$) and $T/t = 0.005$ ($T < T_c$), respectively. Upper panels: Long-range interactions J_1, J_2, and J_3. Lower panels: $J_{\rm NN}$ interactions between C_e^1-C_e^1 and C_b^4-C_e^2 pairs. The corresponding values are listed in Table I.

magnetic moments at the ZZ edges to align ferromagnetically and can be interpreted as the microscopic mechanism driving the system across the AF-to-FI transition. Below T_c, we find $J_{1-3} > 0$ for $\delta = 2$ and $\delta = 3$ and we interpret this as a signature of the competition between the AF and the FI states. Evidence of the coexistence and the cooperation of AF and FM correlations in determining the magnetic state of doped triangular- and linear-chain ZGNFs was already discussed by Chacko *et al.* [21] within exact diagonalization calculations. This hints at the generality of the above scenario in graphene nanostructures, which is not limited to a particular shape but seems to be a general feature related to the presence of ZZ edges. Note, however, that the values of the FM J_{ij} couplings extracted in the calculations are relatively weak compared to the AF $J_{\rm NN}$ and the temperature scale T_c at which FI magnetic order sets in. This suggests that also the geometry of the ZGNF plays an important role, assisting the exchange couplings in the formation of the FI state.

IV. SUMMARY AND OUTLOOK

In this work we have investigated the magnetic properties of a doped ZGNF within the framework of inhomogeneous DMFT. For a half-filled nanoflake we analyze the onset of magnetism as a function of the local interaction U. We identify a dichotomy between bulk and edge C atoms, which persists from weak to strong coupling. Above a threshold value of U, the ground state of the ZGNF is in a fully compensated AF state. The analysis of the energy balance underlying the magnetic state suggests that, for realistic values of the interaction, at half-filling the AF state is stabilized by a potential energy gain characteristic of the weak-coupling mechanism. The results obtained are in qualitative agreement with static MFT and DFT calculations but show that quantum fluctuations suppress, as expected, the AF ordering with respect to mean-field approximations.

Upon introducing charge carriers we observe melting of the AF state. Below a doping-dependent ordering temperature $T_c(\delta)$ it is possible to stabilize a short-range FI order, in which the magnetic moments at the ZZ edges are aligned ferromagnetically. In the FI state the ZGNF displays a net ferromagnetic moment which coexists with a finite staggered magnetization. We interpret the change in the magnetic configuration in terms of an effective magnetic exchange between the ordered spins, mediated by the charge carriers localized in the proximity of the edges.

The possibility of driving FM correlations upon doping has been discussed in the framework of DFT [14] and exact diagonalization [21]. The overall agreement with these studies indicates that a reasonable description of the magnetic phases can already be obtained within a mean-field description of long-range correlations. In this framework, DMFT has allowed us to accurately capture the interplay between the incoherent excitations that form the fluctuating local moment and the coherent low-energy excitations that screen this local moment on longer time scales and mediate the magnetic exchanges which stabilize the ordered state. Moreover, the possibility of describing both the temperature and the doping dependence of the effective exchange couplings sheds some light on the onset of FI short-range order and the strong competition between AF and FM correlations in ZGNFs.

Evidently, any change in the magnetism and in the low-energy spectral properties will have important consequences for the transport through ZGNFs. Hence, the above analysis indicates electrostatic control of the magnetization of doped ZGNF as a promising route towards the future conception and realization of carbon-based spintronic devices.

ACKNOWLEDGMENTS

We acknowledge valuable discussions with R. Drost, D. Prezzi, and Z. Zhong. We are also grateful to G. Sangiovanni for helpful discussions in several stages of this work and to M. Pickem, who provided a benchmark for the static MFT results. We acknowledge financial support from the Austrian Science Fund (FWF) through Erwin Schrödinger Fellowship No. J3890-N36 (A.V.), through Project No. I-610-N16 (A.T.), and the SFB ViCoM F41 (A.T., A.V., K.H.), as well as the European Research Council under the European Union's Seventh Framework Program FP7/ERC through Grant Agreements No. 306447 (K.H., A.V.), No. 240524 (M.C., A.A., A.V.), and No. 280555 (A.A.).

APPENDIX: DETAILS OF THE NUMERICAL SIMULATIONS

In the following we discuss the technical details of the magnetic real-space DMFT calculations and the annealing procedure used to obtain the temperature evolution of the magnetic properties of the ZGNF. The auxiliary AIMs of the real-space DMFT algorithm are solved with a Lánczos exact diagonalization impurity solver [64,65] which is able

to accurately describe the physics both at $T = 0$ and at finite T. We employ a typical discretization of the Hilbert space of $n_s = 1 + n_b = 9$ sites, with n_b being the number of bath sites connected to the impurity. In specific cases we also perform calculations up to $n_s = 12$ sites, finding no qualitative difference in the physical observables. The reliability of the finite-temperature results obtained with the Lánczos exact diagonalization impurity solver was tested against the continuous-time quantum Monte Carlo impurity solver implemented in the w2dynamics package [66], showing quantitative agreement of the physical observables.

In order to get a magnetic solution within real-space DMFT, we lift the local SU(2) spin rotational symmetry of each auxiliary AIM. The symmetry is manually broken at the beginning of the self-consistency cycle by applying a symmetry-breaking feld $\eta_{i\sigma}$ to the spin-dependent DMFT bath $\mathcal{G}_{0i\sigma}(\omega)$. In the case of an AF state, the symmetry-breaking field takes the form

$$\eta_{i\sigma} = \begin{cases} \eta(\delta_{\sigma\uparrow} - \delta_{\sigma\downarrow}) & \text{if } i \in \mathcal{A}, \\ \eta(\delta_{\sigma\downarrow} - \delta_{\sigma\uparrow}) & \text{if } i \in \mathcal{B}, \end{cases} \tag{A1}$$

where δ is the Kronecker symbol, and we typically set the parameter $\eta = 0.05t > 0$. The field in Eq. (A1) corresponds to a staggered perturbation in real space with the same symmetry as the fully compensated AF state.

At half-filling the system is unstable toward antiferromagnetism and the convergence of the DMFT self-consistency is smooth down to $T = 0$. At finite doping ($\delta \neq 0$), instead, besides the solution of the inhomogeneous real-space DMFT equations, also the chemical potential $\mu(n)$ corresponding to the electron concentration $n = \sum_{i\sigma} \langle n_{i\sigma} \rangle$ must be determined. The search for $\mu(n)$ involves a complex root-finding within the self-consistent procedure, which makes the convergence of DMFT numerically unstable for arbitrary values of T and δ. The difficulty of the root-finding is also enhanced due to the discreteness of the energy spectrum for a nanoscopic system. However, motivated by physical observations, it is possible to obtain a reliable self-consistent solution of the DMFT equations over a wide range of T and δ by following an annealing procedure. Indeed, at high T, AF short-range magnetic correlations are dominant, as evidenced by the values of the effective magnetic exchange J_{ij} listed in Table I. The AF correlations stabilize a fully compensated AF state, also at $\delta \neq 0$. A staggered spatial order of the magnetic moments can be easily obtained at high T with the natural choice in Eq. (A1) for $\eta_{i\sigma}$, mainly for two reasons: (i) the magnetic ground state displays a spatial distribution of the magnetic moments that closely resembles the initial state given by the symmetry-breaking field $\eta_{i\sigma}$; and (ii) the temperature-broadening soothes the complexity of the root-finding in the case of a discrete energy spectrum. Once a high-T calculation has converged, the chemical potential μ, the spin-dependent Weiss fields $\mathcal{G}_{0i\sigma}(\omega)$, and the list of Lánczos states for each inequivalent atom are used as input for the calculation at lower T. As the input Weiss field for the next calculation is already symmetry-broken, the annealing procedure is continued *without* imposing a symmetry-breaking field η. In this way, we are able to observe a *spontaneous* transition from the AF to the FI state in the low-T regime. In analogy, a reverse annealing procedure is followed starting from a converged low-T calculation, in order to reveal the hysteretic behavior of the magnetic moments at $\delta \neq 0$.

[1] I. Snook and A. Barnard, in *Graphene Nano-flakes and Nano-dots: Theory, Experiment and Applications, Physics and Applications of Graphene—Theory*, edited by S. Mikhailov (InTech, Rijeka, Croatia, 2011).

[2] Y.-W. Son, M. L. Cohen, and S. G. Louie, Phys. Rev. Lett. **97**, 216803 (2006).

[3] Y. Wang, Y. Huang, Y. Song, X. Zhang, Y. Ma, J. Liang, and Y. Chen, Nano Lett. **9**, 220 (2009).

[4] H. S. S. Ramakrishna Matte, K. S. Subrahmanyam, and C. N. R. Rao, J. Phys. Chem. C **113**, 9982 (2009).

[5] L. Chen, L. Guo, Z. Li, H. Zhang, J. Lin, J. Huang, S. Jin, and X. Chen, Sci. Rep. **3**, 2599 (2013).

[6] G. Z. Magda, X. Jin, I. Hagymási, P. Vancsó, Z. Osváth, P. Nemes-Incze, C. Hwang, L. P. Biró, and L. Tapasztó, Nature **514**, 608 (2014).

[7] R. Drost, S. Kezilebieke, M. M. Ervasti, S. K. Hämäläinen, F. Schulz, A. Harju, and P. Liljeroth, Sci. Rep. **5**, 16741 (2015).

[8] R. Drost, A. Uppstu, F. Schulz, S. K. Hämäläinen, M. Ervasti, A. Harju, and P. Liljeroth, Nano Lett. **14**, 5128 (2014).

[9] I. A. Verzhbitskiy, M. De Corato, A. Ruini, E. Molinari, A. Narita, Y. Hu, M. G. Schwab, M. Bruna, D. Yoon, S. Milana, X. Feng, K. Müllen, A. C. Ferrari, C. Casiraghi, and D. Prezzi, Nano Lett. **16**, 3442 (2016).

[10] Y.-W. Son, M. L. Cohen, and S. G. Louie, Nature **444**, 347 (2006).

[11] W. L. Wang, S. Meng, and E. Kaxiras, Nano Lett. **8**, 241 (2008).

[12] J. Kang, F. Wu, and J. Li, J. Appl. Phys. **112**, 104328 (2012).

[13] W. Sheng, Z. Y. Ning, Z. Q. Yang, and H. Guo, Nanotechnology **21**, 385201 (2010).

[14] M. Kabir and T. Saha-Dasgupta, Phys. Rev. B **90**, 035403 (2014).

[15] J. Fernández-Rossier and J. J. Palacios, Phys. Rev. Lett. **99**, 177204 (2007).

[16] W. L. Wang, O. V. Yazyev, S. Meng, and E. Kaxiras, Phys. Rev. Lett. **102**, 157201 (2009).

[17] M. Grujić, M. Tadić, and F. M. Peeters, Phys. Rev. B **87**, 085434 (2013).

[18] Y. Zhou, Z. Wang, P. Yang, and F. Gao, J. Phys. Chem. C **116**, 7581 (2012).

[19] F. Zou, L. Zhu, and K. Yao, Sci. Rep. **5**, 15966 (2015).

[20] W. Zhang, Sci. Rep. **4**, 6320 (2014).

[21] S. Chacko, D. Nafday, D. G. Kanhere, and T. Saha-Dasgupta, Phys. Rev. B **90**, 155433 (2014).

[22] A. M. Black-Schaffer, Phys. Rev. B **81**, 205416 (2010).

[23] K. Szałowski, Phys. Rev. B **84**, 205409 (2011).

[24] K. Szałowski, Phys. Rev. B **90**, 085410 (2014).

[25] F. M. Hu, T. Ma, H.-Q. Lin, and J. E. Gubernatis, Phys. Rev. B **84**, 075414 (2011).

[26] B. Uchoa, T. G. Rappoport, and A. H. Castro Neto, Phys. Rev. Lett. **106**, 016801 (2011).

[27] H. Feldner, Z. Y. Meng, A. Honecker, D. Cabra, S. Wessel, and F. F. Assaad, Phys. Rev. B **81**, 115416 (2010).
[28] H. Feldner, Z. Y. Meng, T. C. Lang, F. F. Assaad, S. Wessel, and A. Honecker, Phys. Rev. Lett. **106**, 226401 (2011).
[29] S. Dutta and K. Wakabayashi, Sci. Rep. **2**, 519 (2012).
[30] I. Hagymási and Ö. Legeza, Phys. Rev. B **94**, 165147 (2016).
[31] A. Georges, G. Kotliar, W. Krauth, and M. Rozenberg, Rev. Mod. Phys. **68**, 13 (1996).
[32] S. Bhowmick and V. Shenoy, J. Chem. Phys. **128**, 244717 (2008).
[33] A. Kretinin, G. L. Yu, R. Jalil, Y. Cao, F. Withers, A. Mishchenko, M. I. Katsnelson, K. S. Novoselov, A. K. Geim, and F. Guinea, Phys. Rev. B **88**, 165427 (2013).
[34] T. O. Wehling, E. Şaşioğlu, C. Friedrich, A. I. Lichtenstein, M. I. Katsnelson, and S. Blügel, Phys. Rev. Lett. **106**, 236805 (2011).
[35] M. Schüler, M. Rösner, T. O. Wehling, A. I. Lichtenstein, and M. I. Katsnelson, Phys. Rev. Lett. **111**, 036601 (2013).
[36] M. Potthoff and W. Nolting, Phys. Rev. B **59**, 2549 (1999).
[37] S. Florens, Phys. Rev. Lett. **99**, 046402 (2007).
[38] M. Snoek, I. Titvinidze, C. Töke, K. Byczuk, and W. Hofstetter, New J. Phys. **10**, 093008 (2008).
[39] I. Titvinidze, A. Schwabe, N. Rother, and M. Potthoff, Phys. Rev. B **86**, 075141 (2012).
[40] A. Valli, G. Sangiovanni, O. Gunnarsson, A. Toschi, and K. Held, Phys. Rev. Lett. **104**, 246402 (2010).
[41] D. Jacob, K. Haule, and G. Kotliar, Phys. Rev. B **82**, 195115 (2010).
[42] A. Valli, G. Sangiovanni, A. Toschi, and K. Held, Phys. Rev. B **86**, 115418 (2012).
[43] H. Das, G. Sangiovanni, A. Valli, K. Held, and T. Saha-Dasgupta, Phys. Rev. Lett. **107**, 197202 (2011).
[44] A. Valli, H. Das, G. Sangiovanni, T. Saha-Dasgupta, and K. Held, Phys. Rev. B **92**, 115143 (2015).
[45] A. Valli, T. Schäfer, P. Thunström, G. Rohringer, S. Andergassen, G. Sangiovanni, K. Held, and A. Toschi, Phys. Rev. B **91**, 115115 (2015).
[46] A. Toschi, A. A. Katanin, and K. Held, Phys. Rev. B **75**, 045118 (2007).
[47] G. Rohringer, A. Valli, and A. Toschi, Phys. Rev. B **86**, 125114 (2012).
[48] K. A. Ritter and J. W. Lyding, Nat. Mater. **8**, 235 (2009).
[49] W. Hu, L. Lin, C. Yang, and J. Yang, J. Chem. Phys. **141**, 214704 (2014).
[50] A. Toschi, M. Capone, and C. Castellani, Phys. Rev. B **72**, 235118 (2005).
[51] C. Taranto, G. Sangiovanni, K. Held, M. Capone, A. Georges, and A. Toschi, Phys. Rev. B **85**, 085124 (2012).
[52] A. Tagliavini, M. Capone, and A. Toschi, Phys. Rev. B **94**, 155114 (2016).
[53] G. Rohringer and A. Toschi, Phys. Rev. B **94**, 125144 (2016).
[54] S. Sorella and E. Tosatti, Europhys. Lett. **19**, 699 (1992).
[55] S. Sorella, Y. Otsuka, and S. Yunoki, Sci. Rep. **2**, 992 (2012).
[56] H.-S. Tao, Y.-H. Chen, H. F. Lin, H. D. Liu, and W. M. Liu, Sci. Rep. **4**, 5367 (2014).
[57] S. Arya, P. V. Sriluckshmy, S. R. Hassan, and A.-M. S. Tremblay, Phys. Rev. B **92**, 045111 (2015).
[58] M. Sentef, J. Kuneš, P. Werner, and A. P. Kampf, Phys. Rev. B **80**, 155116 (2009).
[59] A. Amaricci, A. Privitera, and M. Capone, Phys. Rev. A **89**, 053604 (2014).
[60] H. S. Moon, J. M. Yun, K. H. Kim, S. S. Jangd, and S. G. Lee, RSC Adv. **6**, 39587 (2016).
[61] G. Rohringer, A. Toschi, A. Katanin, and K. Held, Phys. Rev. Lett. **107**, 256402 (2011).
[62] D. Hirschmeier, H. Hafermann, E. Gull, A. I. Lichtenstein, and A. E. Antipov, Phys. Rev. B **92**, 144409 (2015).
[63] M. I. Katsnelson and A. I. Lichtenstein, Phys. Rev. B **61**, 8906 (2000).
[64] M. Caffarel and W. Krauth, Phys. Rev. Lett. **72**, 1545 (1994).
[65] M. Capone, L. de'Medici, and A. Georges, Phys. Rev. B **76**, 245116 (2007).
[66] N. Parragh, A. Toschi, K. Held, and G. Sangiovanni, Phys. Rev. B **86**, 155158 (2012).